temperature differences exist between the day and night faces of the planet, consistent with a model in which very little horizontal energy transport occurs in the planetary atmosphere. Furthermore, it indicates that the opportunities for direct extrasolar planetary observations are better than previously thought, because useful data can be obtained even in cases where the planetary orbit is not so fortuitously aligned that the system exhibits transits or eclipses.

References and Notes

1. D. Deming, S. Seager, L. J. Richardson, J. Harrington, *Nature* **434**, 740 (2005).
2. D. Charbonneau *et al.*, *Astrophys. J.* **626**, 523 (2005).
3. There is no official terminology for planets that orbit close to their parent stars. The term "hot Jupiter" is the most common, although some authors have adopted other terms, such as "Pegasids," "Pegasi planets," or "Roasters."
4. G. H. Rieke *et al.*, *Proc. SPIE* **5487**, 50 (2004).
5. M. W. Werner *et al.*, *Astrophys. J. Suppl. Ser.* **154**, 1 (2004).
6. K. Horne, *Publ. Astron. Soc. Pac.* **98**, 609 (1986).
7. L. J. Richardson, J. Harrington, S. Seager, D. Deming, *Astrophys. J.*; preprint available at http://arxiv.org/abs/astro-ph/0606096.
8. The passage of an extrasolar planet behind its star, an eclipse, results in a drop in the total system flux. This allows a measurement of the absolute flux emerging from the part of the planet that faces the star (the day side). This is possible when the orbit is aligned almost edge-on to the line of sight.
9. D. Deming, J. Harrington, S. Seager, L. J. Richardson, *Astrophys. J.* **644**, 560 (2006).
10. We use the estimator provided by the Spitzer Science Center, which is based on the DIRBE model described by (*21*). Further information on the specific implementation is given at http://ssc.Spitzer.caltech.edu/documents/background.
11. R. P. Butler *et al.*, *Astrophys. J.* **474**, L115 (1997).
12. J. Cho, K. Menou, B. Hansen, S. Seager, *Astrophys. J.* **587**, L117 (2003).
13. C. S. Cooper, A. P. Showman, *Astrophys. J.* **629**, L45 (2005).
14. G. W. Henry, S. L. Baliunas, R. A. Donahue, F. C. Fekel, W. Soon, *Astrophys. J.* **531**, 415 (2000).
15. E. Shkolnik, G. A. H. Walker, D. A. Bohlender, P.-G. Gu, M. Kürster, *Astrophys. J.* **622**, 1075 (2005).
16. S. Seager *et al.*, *Astrophys. J.* **632**, 1122 (2005).
17. T. Barman, P. Hauschildt, F. Allard, *Astrophys. J.* **632**, 1132 (2005).
18. J. Fortney, M. Marley, K. Lodders, D. Saumon, R. Freedman, *Astrophys. J.* **627**, L69 (2005).
19. A. Burrows, I. Hubeny, D. Sudarsky, *Astrophys. J.* **625**, L135 (2005).
20. D. A. Fischer, J. Valenti, *Astrophys. J.* **622**, 1102 (2005).
21. T. Kelsall *et al.*, *Astrophys. J.* **508**, 44 (1998).
22. The usual estimate given for planetary temperatures is the equilibrium temperature, T_{eq}, defined as the effective temperature of a uniformly bright planet radiating energy at a rate that balances the irradiation received from the star. T_{eq} is thus determined by the stellar effective temperature, T_{eff}, stellar radius, R_*, and distance of the planet from the star a:

$$T_{eq} = 1744 \text{ K} (T_{eff}/6212 \text{ K})(R_*/1.57R_\odot)^{1/2}$$
$$\times (a/0.059 \text{AU})^{-1/2}$$

in the case of υ and b with albedo = 0.05. However, in a proper no-redistribution model, the temperature distribution is not uniform but rather hottest at the substellar point and coolest at the limb, and the full-phase temperature average over the planetary surface is better approximated by $(4/3)^{1/4}T_{eq}$. This is the temperature we adopt, which is 1875 K in this case.
23. This work is based on observations made with the Spitzer Space Telescope, which is operated by the Jet Propulsion Laboratory, California Institute of Technology, under contract with NASA. Support for this work was provided directly by NASA, its Origins of Solar Systems and Astrophysical Theory programs, as well as the Astrobiology Institute and Spitzer Science Center. We thank the personnel of the Spitzer Science Center and its MIPS instrument, who ultimately made these measurements possible.

Brownian Motion of an Ellipsoid

Y. Han,[1] A. M. Alsayed,[1] M. Nobili,[2] J. Zhang,[1] T. C. Lubensky,[1]* A. G. Yodh[1]

We studied the Brownian motion of isolated ellipsoidal particles in water confined to two dimensions and elucidated the effects of coupling between rotational and translational motion. By using digital video microscopy, we quantified the crossover from short-time anisotropic to long-time isotropic diffusion and directly measured probability distributions functions for displacements. We confirmed and interpreted our measurements by using Langevin theory and numerical simulations. Our theory and observations provide insights into fundamental diffusive processes, which are potentially useful for understanding transport in membranes and for understanding the motions of anisotropic macromolecules.

Brownian motion (*1*), wherein small particles suspended in a fluid undergo continuous random displacements, has fascinated scientists since before it was first investigated by the botanist Robert Brown in the early 19th century. The origin of this mysterious motion was largely unexplained until Einstein's famous 1905 paper (*2*) that established a relation between the diffusion coefficient of a Brownian particle and its friction coefficient. One year later (*3*), Einstein extended the concept of Brownian dynamics to rotational and other degrees of freedom. The subsequent study of Brownian motion and its generalizations has had a profound impact on physics, mathematics, chemistry, and biology (*4*). Because direct detection of translational Brownian motion is relatively easy, many exper-

iments elucidating the ideas of translational diffusion have been carried out. On the other hand, the direct visualization of rotational Brownian motion has not been an easy task, and fundamental concepts about motions of anisotropic macromolecules remain untested. For this contribution, we used digital video microscopy to study the Brownian motion of an isolated ellipsoid in suspension and thus directly observed the coupling effects between rotational and translational motion.

Particle anisotropy leads to dissipative coupling of translational to rotational motion and to physics first explored by F. Perrin (*5*, *6*). A uniaxial anisotropic particle is characterized by two translational hydrodynamic friction coefficients, γ_a and γ_b, respectively, for motion parallel and perpendicular to its long axis. If a particle's rotation is prohibited, it will diffuse independently in directions parallel and perpendicular to its long axis with respective diffusion constants of $D_\alpha = k_B T/\gamma_\alpha$ for α either a or b, where k_B is Boltzmann's constant and T is the temperature. In general, γ_a is less than γ_b (*7*), and consequently D_a is greater than D_b. If

rotation is allowed, rotational diffusion, characterized in two dimensions by a single diffusion coefficient, D_θ, and associated diffusion time, $\tau_\theta = 1/(2D_\theta)$, washes out directional memory and leads to a crossover from anisotropic diffusion at short times to isotropic diffusion at times much longer than τ_θ. Figure 1, A and B, presents numerical simulations (*8*) that illustrate this behavior. Our experiments, which were restricted to two dimensions (2D), provide explicit verification of this behavior and some of its extensions. In addition, we show that a fundamental property of systems with dissipatively coupled translation and rotation is the existence of non-Gaussian probability density functions (PDFs) for displacements in the lab frame.

Micrometer-sized PMMA (polymethyl methacrylate) uniaxial ellipsoids (*9*) were under strong quasi–two-dimensional confinement in a thin glass cell. The choice of 2D rather than 3D for these studies substantially simplified the experimental imaging tasks as well as the data acquisition time and storage requirements. The choice also ensured that the measured effects would be large by virtue of the much larger friction anisotropy in 2D compared with 3D. The local cell thickness was ~1 μm. It was measured to within 0.1 μm resolution by comparing the Michel-Levy chart (*10*) to the reflected interference colors produced by the two inner surfaces under white light illumination on the microscope (Fig. 1D). To avoid interactions between ellipsoids, we made the solution very dilute. The Brownian motion of a single ellipsoid in water was recorded by a charge-coupled device (CCD) camera on a videotape at 30 frame/s. From the image analyses, we obtained data sets consisting of a particle's center-of-mass positions

[1]Department of Physics and Astronomy, University of Pennsylvania, 209 South 33rd Street, Philadelphia, PA 19104, USA. [2]Laboratoire des Colloides, Verres et Nanomateriaux CNRS-University Montpellier II, Place E. Bataillon, 34090 Montpellier, France.
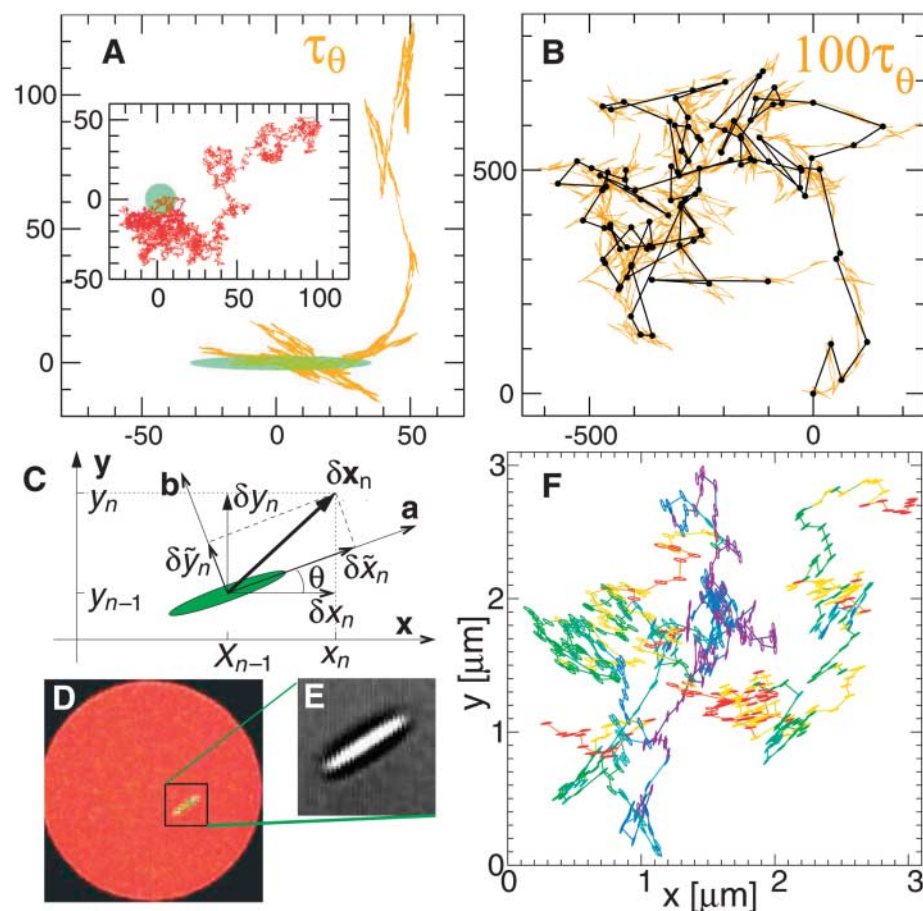
*To whom correspondence should be addressed. E-mail: tom@physics.upenn.edu

$\mathbf{x}(t_n) = [x(t_n), y(t_n)]$ in the lab frame and its orientation angles $\theta(t_n)$ relative to the x axis at times $t_n = n(1/30)$ s, as shown in Fig. 1F. The orientational resolution is 1°, and spatial resolutions are 0.5 pixel = 40 nm along the particle's short axis and only 0.8 pixel along its long axis because of the superimposed small tumbling motion. We define each 1/30-s time interval as a step. During the nth step, the particle's position changes by $\delta\mathbf{x}(t_n) = \mathbf{x}(t_n) - \mathbf{x}(t_{n-1})$ and its angle by $\delta\theta(t_n) = \theta(t_n) - \theta(t_{n-1})$. From the data set, we extract an ensemble of particle trajectories starting at different times τ_0 and ending a time t later. The total positional and angular displacements in these trajectories are, respectively, $\Delta\mathbf{x}(t) = \mathbf{x}(t + \tau_0) - \mathbf{x}(\tau_0)$ and $\Delta\theta(t) = \theta(t + \tau_0) - \theta(\tau_0)$.

We first consider the statistical properties of $\theta(t)$, which, as pointed out by Perrin (6), are independent of translational motions. We measured data from a 30-min trajectory of a 2.4 μm–by–0.3 μm–by–0.3 μm ellipsoid confined in an 846-nm-thick cell (Fig. 2A). The inset shows that the mean-square angular displacement $\langle[\Delta\theta(t)]^2\rangle$ equals $2D_\theta t$, where the average $\langle \ \rangle$ is over all trajectories with different starting times τ_0. The mean-square angular displacement has diffusive behavior over the entire range of observable times with a rotational time of $\tau_\theta = 1/(2D_\theta) = 3.1$ s. Over the time scales we can observe, this diffusive behavior is independent of θ_0. The PDF for $\Delta\theta(t)$ was measured to be Gaussian with variance $2D_\theta t$, and the angles $\theta(t)$ were measured to be uniformly distributed in $[0,2\pi]$.

We now turn to the statistics of translational motion whose full understanding is facilitated by the consideration of decomposing the displacement $\delta\mathbf{x}_n$ into its components $\delta\tilde{x}_{ni}$ relative to the body frame or δx_{ni} relative to the fixed lab frame. As shown in Fig. 1C, the two are related via a rotation, $\delta\tilde{x}_{ni} = R_{ij}\delta x_{nj}$, where the Einstein summation convention over repeated indices is understood and $R_{ij} = \begin{pmatrix} \cos\theta_n & \sin\theta_n \\ -\sin\theta_n & \cos\theta_n \end{pmatrix}$ is the rotation matrix with $\theta_n = [\theta(t_{n-1}) + \theta(t_n)]/2$. In practice, choosing $\theta_n = \theta(t_{n-1})$ or $\theta_n = \theta(t_n)$ has little effect on our results because θ barely changes during 1/30 s. We can construct total body-frame displacements by summing over displacements in each step, $\tilde{x}(t_n) = \sum_{k=1}^n \delta\tilde{x}_k$, and from $\tilde{x}(t_n)$ we can construct body-frame displacements for trajectories of duration t at starting time τ_0 via $\Delta\tilde{x}(t) = \tilde{x}(t + \tau_0) - \tilde{x}(\tau_0)$.

Mean-square displacements (MSDs) in the body frame and in the lab frame were averaged over all trajectories with different initial angle $\theta_0 \equiv \theta(\tau_0)$ (Fig. 2A). They are all diffusive with $\langle[\Delta\tilde{x}(t)]^2\rangle = 2D_a t$, $\langle[\Delta\tilde{y}(t)]^2\rangle = 2D_b t$, and $\langle[\Delta x(t)]^2\rangle = \langle[\Delta y(t)]^2\rangle = (D_a + D_b)t \equiv 2\overline{D}t$. The full average $\langle \ \rangle$ for any observable A can be viewed as an ensemble average of trajectories at fixed θ_0 followed by a second average over all θ_0: $\langle A \rangle = [\langle A \rangle_{\theta_0}]_{av} = \frac{1}{2\pi}\int_0^{2\pi} d\theta_0 \langle A \rangle_{\theta_0}$.

A particle with a given initial angle will diffuse more rapidly along its long axis than along its short axis. As time progresses, however, memory of its initial direction is lost, and diffusion becomes isotropic. Thus, averages over trajectories at fixed θ_0 should exhibit a crossover from early-time anisotropic to late-time isotropic diffusion. Our measurements with $\theta_0 = 0$ of the time-dependent diffusion coefficients $D_{xx}(t) = \langle[\Delta x(t)]^2\rangle_0/(2t)$ and $D_{yy}(t) = \langle[\Delta y(t)]^2\rangle_0/(2t) = \langle[\Delta x(t)]^2\rangle_{\frac{\pi}{2}}/(2t)$ provide direct verification of this crossover (Fig. 2B): At $t \ll \tau_\theta$, D_{xx} equals D_a and D_{yy} equals D_b, whereas for $t \gg \tau_\theta$, D_{xx} equals D_{yy} equals $\overline{D}$.

The anisotropic-to-isotropic crossover was calculated in 3D by Perrin (6) and is mentioned in qualitative terms in a 3D simulation (11). We calculate the properties of this transition in 2D within the Langevin formalism and compare them with experiment. Because our time scales are much larger than the momentum relaxation times of a micrometer-sized particle in water ($I/\gamma_{rot} \sim m/\gamma \sim 10^{-7}$ s), we can ignore inertial terms. The Langevin equations for displacement and angle in the lab frame in the presence of external forces described by a Hamiltonian H are

$$\partial_t x_i = -\Gamma_{ij}(\theta)\frac{\partial H}{\partial x_j} + \xi_i(t) \qquad (1a)$$

$$\partial_t \theta = -\Gamma_\theta \frac{\partial H}{\partial \theta} + \xi_\theta \qquad (1b)$$

where $i = x, y$ for 2D and $\Gamma_{ij} = \gamma_{ij}^{-1}$ is the mobility tensor, which can be expressed in terms of the unit vector $\mathbf{n}(t) \equiv \mathbf{n}[\theta(t)]$ specifying the direction of the local anisotropy axis as $\Gamma_{ij}(t) = \Gamma_b\delta_{ij} + \Delta\Gamma n_i(t)n_j(t) = \Gamma\delta_{ij} + \Delta\Gamma M_{ij}[\theta(t)]/2$, where $\Gamma = (\Gamma_a + \Gamma_b)/2$, $\Delta\Gamma = \Gamma_a - \Gamma_b$, and $M_{ij}(\theta) = \begin{pmatrix} \cos 2\theta & \sin 2\theta \\ \sin 2\theta & -\cos 2\theta \end{pmatrix}$. $\xi_\theta(t)$ and $\xi_i(t)$ are ran-

Fig. 1. (**A** and **B**) 10,000-step 2D random walk trajectories for an ellipsoid with $D_a = 0.99$ and $D_b = 0.01$ during τ_θ and $100\tau_\theta$, respectively. τ_θ is the time for the ellipsoid to diffuse 1 rad. (A Inset) 10,000-step trajectory for a sphere with $D_a = D_b = 0.5$ during τ_θ. The initial positions are represented by a green ellipse and a sphere. At step times long compared with τ_θ, the coarse-grained 100-step black trajectory in (B) is similar to that of the random walk of a spherical particle in fig. S1. (**C**) Representation of an ellipsoid in the x-y lab frame and the $\tilde{x}$-$\tilde{y}$ body frame. The angle between two frames is $\theta(t)$. The displacement $\delta\mathbf{x}$ can be decomposed as $(\delta x, \delta y)$ or $(\delta\tilde{x}, \delta\tilde{y})$. (**D**) True interference color in the reflection mode of the microscope. (**E**) Ellipsoid image in the transmission mode. (**F**) A typical 20-s experimental trajectory with step 1/30 s. $D_a/D_b = 4.07$. Orientations are further labeled with a rainbow color scale. For example, the purple parts of the trajectory reflect a higher mobility along the y direction, and the red parts reflect a higher mobility along the x direction.

dom noise sources with zero mean and respective variances, $\langle \xi_\theta(t)\xi_\theta(t') \rangle = 2k_B T\Gamma_\theta \delta(t - t') = 2D_\theta \delta(t - t')$ and $\langle \xi_i(t)\xi_j(t') \rangle_{\theta(t)} = 2k_B T\Gamma_{ij}[\theta(t)]\delta(t - t')$, dictated by the Einstein relation or equivalently by the requirement that thermal equilibrium be reached at long times. We retain H in Eq. 1 even though the external forces are zero in our experiments to emphasize that the mobilities Γ_{ij} and Γ_θ relating velocity and angular velocity to force and torque, respectively, determine the variances of the random noise sources. $\xi_\theta(t)$ obeys Gaussian statistics at all times, as does $\xi_i(t)$ for a fixed angle $\theta(t)$. The average $\langle A \rangle_{\theta_0}$ of any measurable quantity is equivalent to the average of A over both $\xi_i(t)$ and $\xi_\theta(t)$ at fixed θ_0.

Because there are no external forces in our experiments, we can set $\partial H/\partial x = 0$ and $\partial H/\partial\theta = 0$. Equation 1b for $\theta(t)$ is simply the Langevin equation for 1D diffusion. It yields a time-independent diffusion coefficient $D_\theta = \langle[\Delta\theta(t)]^2\rangle/(2t)$, a Gaussian PDF for $\Delta\theta(t)$ with variance $2D_\theta t$, and consequently $\langle\cos n\Delta\theta(t)\rangle = \mathrm{Re}\langle e^{in\Delta\theta(t)}\rangle = \cos n\theta_0 e^{-n^2 D_\theta t}$. From this we can calculate (8) the time-dependent displacement diffusion tensor for fixed θ_0:

$$D_{ij}(t,\theta_0) = \langle[\Delta x_i(t)][\Delta x_j(t)]\rangle_{\theta_0}/(2t)$$
$$= \overline{D}\delta_{ij} + \frac{\Delta D}{2}\frac{\tau_4(t)}{t}M_{ij}(\theta_0) \qquad (2)$$

where $\Delta D \equiv D_a - D_b$ and $\tau_n(t) \equiv \int_0^t dt' e^{-nD_\theta t'} = (1 - e^{-nD_\theta t})/(nD_\theta)$. $D_{xx}(t,0)$ and $D_{yy}(t,0)$ quantitatively match experimental results for $\theta_0 = 0$ as shown in Fig. 2B, with D_a, D_b, and D_θ equal to their values obtained from Fig. 2A. The average of $D_{ij}(t,\theta_0)$ in Eq. 2 over initial angles θ_0 yields $D_{xx} = D_{yy} = D$, in agreement with the MSDs of x and y in Fig. 2A. The 3D counterpart, $D_{xx} = D_{yy} = D_{zz} = (D_a + D_b + D_c)/3$, is widely used in dynamic light scattering (12).

Unlike spheres, anisotropic particles have anisotropic friction coefficients that are responsible for the coupling of translation and rotation. This coupling leads to nontrivial mixed correlation functions such as

$$\langle\Delta x_i \Delta x_j e^{in\theta}\rangle/t =$$
$$[2D + \Delta D A_{ij}^{(n)}(t)/2\,e^{in\theta_0 - n^2 D_\theta t} \qquad (3)$$

where $A^{(n)}{}_{ij}(t) = e^{i2\theta}\tau_{(4+4n)}\begin{pmatrix}1 & -i\\-i & -1\end{pmatrix} + e^{-i2\theta}\tau_{(4-4n)}\begin{pmatrix}1 & i\\i & -1\end{pmatrix}$. Equation 3 is obtained from our Langevin formalism (8). Experimental results agree well with these theoretical predictions and deviate from the theoretical dashed curves obtained assuming translational and rotational motion are decoupled (Fig. 2C).

Transforming Eq. 1a into the body frame at $\partial H/\partial x = 0$, we obtain

$$\partial_t\tilde{x}_i = \tilde{\xi}_i(t) = R_{ij}[\theta(t)]\xi_j(t) \qquad (4)$$

The probability distribution of $\tilde{\xi}_i(t)$, which can be calculated directly from its definition and the properties of $\xi_i(t)$, is a Gaussian with zero mean and variance $\langle\tilde{\xi}_i\tilde{\xi}_j\rangle = 2k_B T\tilde{\Gamma}_{ij}\delta(t - t')$, where $\tilde{\Gamma}_{ij}$ is a $\theta(t)$-independent diagonal matrix with components $\tilde{\Gamma}_{xx} = \Gamma_a$ and $\tilde{\Gamma}_{yy} = \Gamma_b$. Thus, $\langle(\Delta\tilde{x}_i)^2\rangle$ equals $2D_i t$, where $D_i = (D_a, D_b)$, in agreement with the experimental data in Fig. 2A. Because $\tilde{\xi}_i$ is Gaussian, the PDF for body-frame displacements $\Delta\tilde{x}_i(t)$ is Gaussian at all times:

$$f_{\Delta\tilde{x}_i}(x,t) = \frac{1}{\sqrt{2\pi}\sigma_i(t)}e^{-\frac{x^2}{2\sigma_i^2(t)}} \qquad (5)$$

where $\sigma_i^2(t) = 2D_i t$. Our measurements confirm this behavior in fig. S1. For our quasi-2D sample, the ellipsoid's friction and diffusion tensors are different at different heights within the cell (13). Therefore, the PDF of $\Delta\tilde{x}_i$ should be an average of Gaussian PDFs with different variances. However, the interference color from the ellipsoid changed very little throughout the course of our experiment;

from this result we estimate that the ellipsoid remains within 50 nm of the midplane of the cell and that the non-Gaussian effects are too small to be observable as is confirmed by our measurements.

Although the statistics of displacements in the body frame are Gaussian, those in the lab frame are not because of coupling between translation and rotation (14). Prager (15) calculated the non-Gaussian concentration for averaged initial angles in a particular geometry in three dimensions. The lab-frame noise, $\xi_i(t) = R_{ij}^{-1}[\theta(t)]\,\tilde{\xi}_i(t)$, is a nonlinear function of the independent noises $\xi_\theta(t)$ and $\tilde{\xi}_i(t)$. Thus, although its probability distribution is Gaussian for fixed $\theta(t)$ and thus fixed $\xi_\theta(t)$, its distribution averaged over $\xi_\theta(t)$ is non-Gaussian, as is that for $\Delta x_i(t)$. At short times, the lab- and body-frame displacements are equal, and the PDF for $\Delta x_i(t)$ is Gaussian because that for $\Delta\tilde{x}_i(t)$ is. Directional information is lost at times greater than τ_θ. Therefore, at long times, $\Delta\mathbf{x}(t)$ is a sum of displacements from $\sim t/\tau_\theta$ statistically independent steps, and the central limit theorem implies that its PDF is Gaussian. Thus at fixed θ_0, we expect deviation from Gaussian behavior to vanish at $t = 0$ and $t = \infty$ and to reach a maximum at times of order τ_θ.

The simplest manifestations of non-Gaussian behavior are the nonzero values of the fourth- or higher-order cumulants of lab-frame displacements, which can be calculated (8) from our Langevin theory. For example, the fourth cumulant of $\Delta x(t)$ for fixed initial orientation is

$$C_{\theta_0}^{(4)}(t) = \langle[\Delta x(t)]^4\rangle_{\theta_0} - 3\langle[\Delta x(t)]^2\rangle_{\theta_0}^2$$
$$= \frac{1}{2}(\Delta D)^2\Big\{3[\tau_\theta t - \tau_\theta\tau_4(t) - \tau_4(t)^2] +$$
$$[\tau_\theta\tau_4(t) - \tau_\theta\tau_{16}(t) - 3\tau_4(t)^2]\cos 4\theta_0\Big\}$$
$$(6)$$
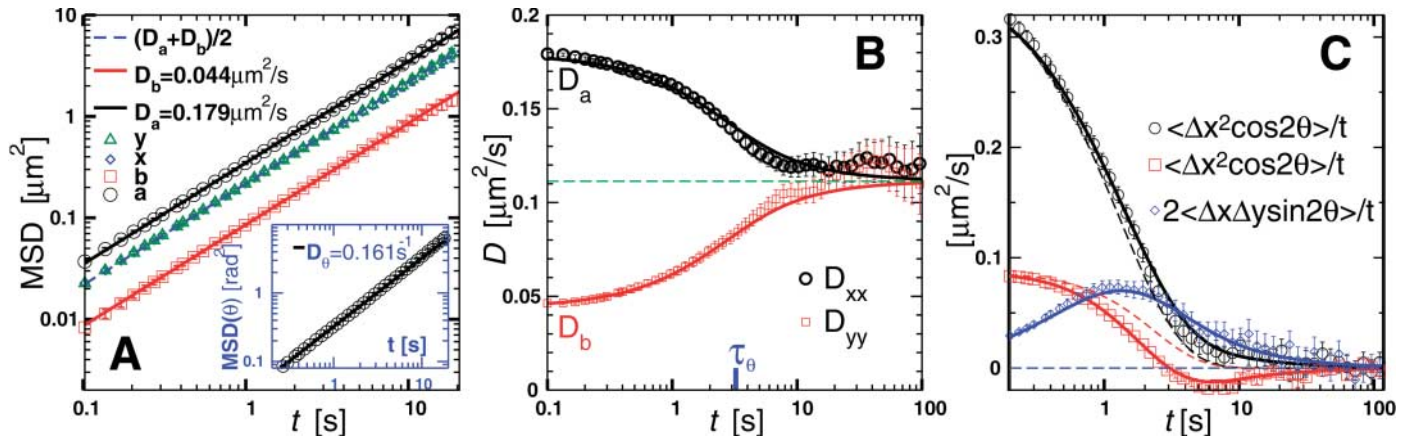
Fig. 2. (**A**) MSDs along a, b, x, and y axes. (Inset) Angular MSD. All curves have diffusive behavior ($\propto t$), and corresponding diffusion coefficients $D = \mathrm{MSD}/(2t)$ shown in the figure are from best fits. (**B**) Diffusion coefficients D in the lab frame. The initial orientation of each trajectory was chosen to be along the x axis ($\theta_0 = 0$), so that D_{xx} and D_{yy} change from D_a and D_b to D, respectively, over time interval τ_θ. Symbols, experiment; error bars $\propto \sqrt{t}$. Solid curves, Eq. 2 when $\theta_0 = 0$. (**C**) Mixed correlations of translational displacements and orientation. Symbols, experiment. Error bars $\propto \sqrt{t}$. Solid curves, theoretical results from Eq. 3 for $n = 2$. Dashed curves, reference uncorrelated averages $\langle\Delta x^2\rangle\langle\cos 2\theta\rangle/t$, $\langle\Delta y^2\rangle\langle\cos 2\theta\rangle/t$, and $2\langle\Delta x\Delta y\rangle\langle\sin 2\theta\rangle/t = 0$.

This function vanishes as t^{2+s_2}, where $s_2 > 0$, as $t \to 0$ and grows linearly in t as $t \to \infty$. The non-Gaussian parameter,

$$p(t,\theta_0) = \frac{C^{(4)}_{\theta_0}(t)}{3\langle[\Delta x(t)]^2\rangle^2_{\theta_0}}$$

$$= \frac{C^{(4)}_{\theta_0}(t)}{3[2\,Dt + \Delta D\tau_4(t)\cos2\theta_0]^2} \qquad (7)$$

vanishes with t^{s_2} for $t \to 0$ and as t^{-1} as $t \to \infty$. The angle-averaged non-Gaussian parameter,

$$\bar{p}(t) = \frac{\overline{C}^{(4)}(t)}{3\langle[\Delta x(t)]^2\rangle^2} = \frac{\Delta D^2}{8\overline{D}^2}\frac{\tau_\theta[t - t_4(t)]}{t^2} \qquad (8)$$

$$\xrightarrow{t\to0} \frac{(D_a/D_b - 1)^2}{2(D_a/D_b + 1)^2} \qquad (9)$$

where $\overline{C}^{(4)}(t) = \langle[\Delta x(t)]^4\rangle - 3\langle[\Delta x(t)]^2\rangle^2$, approaches a constant as $t \to 0$ and vanishes as t^{-1} as $t \to \infty$. Because statistics in the body frame are Gaussian, the body-frame non-Gaussian parameter $p_b(t)$ is zero.

Equations 7 and 8 are confirmed numerically in Fig. 3A. Experimental measurements of both $p(t,\theta_0)$ and $p(t)$ have poor statistics at large t because their errors grow as $t^{3/2}$. Nevertheless, we were able to extrapolate to the $t \to 0$ limit of $p(t)$ in seven samples with different aspect ratios and to confirm Eq. 9 in the Fig. 3A inset. Figure 3A confirms our qualitative expectations about the non-Gaussian parameter p in different frames and for different types of averages, specifically: (i) in the ensemble with fixed θ_0, the non-Gaussian parameter vanishes for $t \ll \tau_\theta$ and $t \gg \tau_\theta$ and reaches a maximum when $t \sim \tau_\theta$; (ii) in the ensemble that averages over θ_0, the non-Gaussian parameter is a maximum at $t = 0$

and vanishes for $t \gg \tau_\theta$; and (iii) larger D_a/D_b causes larger non-Gaussian effects.

It is clear from Eqs. 6 to 9 that non-Gaussian behavior originates in particle anisotropy and vanishes when ΔD vanishes. Thus, non-Gaussian effects for anisotropic particles diffusing in 3D with stick boundary conditions should be small because $1 < D_a/D_b = \gamma_b/\gamma_a < 2$ when $1 < a/b < \infty$ (5, 7). For some small molecules, the slip boundary condition is more appropriate (16, 17) and γ_b/γ_a diverges (11) even in 3D. Under quasi-2D conditions with stick boundary conditions, however, D_a/D_b increases with aspect ratio and finally saturates (13) at a value much larger than 2. In summary, non-Gaussian effects are strong when $D_a \gg D_b$, i.e., for particles with a high aspect ratio confined in quasi-2D (in our case, D_a/D_b reaches about 4) or for some molecules with slip boundary conditions.

Lastly, we consider the lab-frame PDF for $\Delta x(t)$. The expectation is that these PDFs at fixed θ_0 will be non-Gaussian and exhibit maximum deviations from Gaussian behavior at times of order τ_θ. We have verified that this is the case within our statistical errors, but the deviations are very small. The lab-frame PDF averaged over θ_0 shows more striking deviations from Gaussian behavior (8), particularly as $t \to 0$:

$$f_{\Delta x}(x) = \langle\delta[x - \Delta x(t)]\rangle \xrightarrow{t\to0} \int_0^{2\pi}\frac{d\theta}{2\pi}\frac{e^{-\frac{x^2}{2\sigma^2(\theta)}}}{\sqrt{2\pi}\sigma(\theta)} \qquad (10)$$
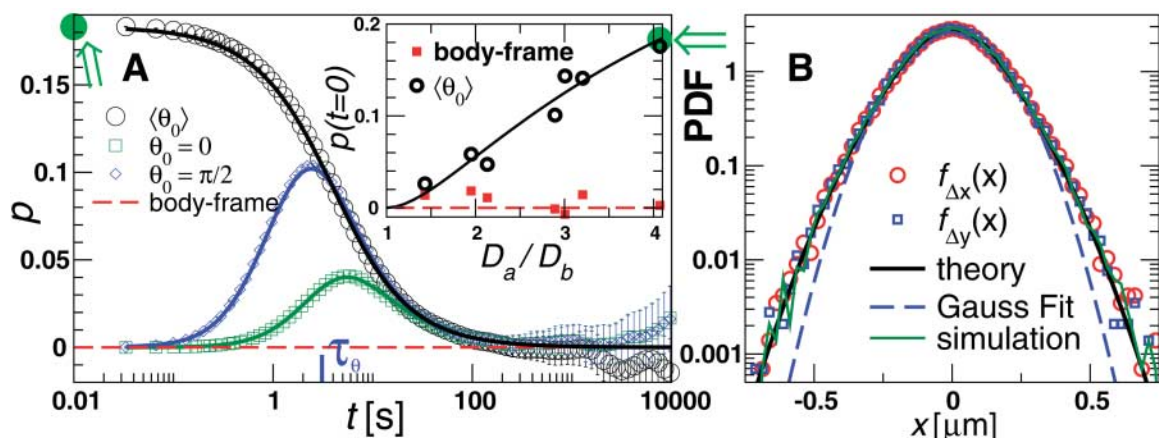
where $\sigma^2(\theta) = \sigma_a^2\cos^2\theta + \sigma_b^2\sin^2\theta$ with $\sigma_i^2 = 2D_it$. The physical meaning of Eq. 10 is apparent. When $t \to 0$, the orientation θ does not change during the displacement. Those Δx with the same θ_0 follow a Gaussian distribution with $\sigma = \sigma(\theta_0)$ because the hydrodynamic drag coefficient $\gamma(\theta_0)$ is a constant. Averaging Gaussian PDFs with different θ_0 over $[0,2\pi]$ yields a non-Gaussian PDF as shown in Eq. 10.

Experimental angle-averaged PDFs of lab-frame displacement are shown (Fig. 3B) at time intervals of $t = 0.1$ s. The system's isotropy is confirmed by $f_{\Delta x}(x) = f_{\Delta y}(x)$. Interestingly, there are more tiny and large steps and fewer middle-sized steps than there are in a Gaussian distribution (fig. S2). This PDF agrees with Eq. 10 very well with no free parameters. We measured the PDFs of 15 samples with different aspect ratios at different confinements. All agreed with Eq. 10. When $D_a/D_b < 2.5$, the measured non-Gaussian PDF becomes indistinguishable from a Gaussian distribution.

The most common experimental probes typically measure only second moments, from which diffusion coefficients can be extracted, that provide no information about non-Gaussian behavior. For example, dynamic light scattering (12, 18) and nuclear magnetic resonance (NMR) (19) measure θ_0-averaged translational diffusion coefficients of anisotropic constituents; and NMR (19), fluorescence depolarization (20), electric birefringence (21), dichroism (22), and depolarized dynamic light scattering (19) measure rotational diffusion coefficients. In principle, some of these probes, light scattering in particular, could provide a measure of $\overline{C}^{(4)}(t) \xrightarrow{t\to0} 3(\Delta D)^2t^2/2$ and higher moments, but we are not aware of any such measurements. Certainly, the non-Gaussian effects would be very small, especially for particles in 3D where $D_a/D_b < 2$.

Our observations using digital video microscopy of the Brownian motion of an isolated ellipsoid in two-dimensions provide exquisitely detailed information about the diffusive properties of anisotropic objects and the subtle interplay between orientational and translational motions. Besides providing us with new insights about a fundamental phenomenon, these observations and underlying theory are potentially useful for research on diffusion of anisotropic molecules in membranes (16), on the hydrodynamics and kinetics of ensembles of anisotropic particles, and on anisotropic molecules that

Fig. 3. (**A**) Non-Gaussian parameters as a function of t. Symbols, simulation in the lab frame for an ellipsoid with D_a, D_b, and D_θ from Fig. 2A. Error bars $\propto t^{3/2}$. Curves, theoretical predictions for $p(t,0)$ and $p(t,\pi/2)$ in Eq. 7 and $p(t)$ in Eq. 8. Dashed line, $p_b(t) = 0$ in the body frame. (Inset) $p(t=0)$ for ellipsoids with different aspect ratios and confinements. Symbols, experiments; curve, theoretical prediction of Eq. 9. The double arrows in the figure and the inset indicate equivalent points for which PDFs are shown in (B). (**B**) Lab-frame PDFs for $\Delta x(t)$ and $\Delta y(t)$ at $t = 0.1$ s. Measured $f_{\Delta x}(x)$ (open circles) and $f_{\Delta y}(x)$ (open squares) agree with the theory (solid dark curve) of Eq. 10 with no free parameter ($\sigma_a = \sqrt{2D_at}$, with D_a from the fit of Fig. 2A). Dashed curve, best Gaussian fit; light curve, simulation.

experience slip boundary conditions and thus have a large ratio of γ_a to γ_b.

References and Notes

1. E. Nelson, *Dynamical Theories of Brownian Motion* (Princeton Univ. Press, Princeton, NJ, 1972).
2. A. Einstein, *Ann. Phys.* **17**, 549 (1905).
3. A. Einstein, *Ann. Phys.* **19**, 289 (1906).
4. E.g., W. T. Coffey, Y. P. Kalmykov, T. J. Waldron, *The Langevin Equation: With Applications to Stochastic Problems in Physics, Chemistry and Electrical Engineering* (World Scientific, Singapore, ed. 2, 2004).
5. F. Perrin, *J. Phys. Radium* **V**, 497 (1934).
6. F. Perrin, *J. Phys. Radium* **VII**, 1 (1936).
7. J. Happel, H. Brenner, *Low Reynolds Number Hydrodynamics* (Kluwer, Dordrecht, Netherlands, 1991).
8. See the Supporting Online Materials of *Science*.
9. C. C. Ho, A. Keller, J. A. Odell, R. H. Ottewill, *Colloid Polym. Sci.* **271**, 469 (1993).
10. N. H. Hartshorne, A. Stuart, *Crystals and the Polarising Microscope* (Edward Arnold, London, ed. 4, 1970).
11. R. Vasanthi, S. Ravichandran, B. Bagchi, *J. Chem. Phys.* **114**, 7989 (2001).
12. B. J. Berne, R. Pecora, *Dynamic Light Scattering* (Dover, New York, 2000).
13. S. Bhattacharya, J. Blawzdziewicz, E. Wajnryb, *J. Fluid Mech.* **541**, 263 (2005).
14. M. Doi, S. F. Edwards, in *The Theory of Polymer Dynamics* (Oxford Univ. Press, Oxford, 1986), p. 300.
15. S. Prager, *J. Chem. Phys.* **23**, 2404 (1955).
16. P. G. Saffman, M. Delbruck, *Proc. Natl. Acad. Sci. U.S.A.* **72**, 3111 (1975).
17. C. M. Hu, R. Zwanzig, *J. Chem. Phys.* **60**, 4354 (1974).
18. D. W. Schaefer, G. B. Benedek, P. Schofield, E. Bradford, *J. Chem. Phys.* **55**, 3884 (1971).
19. W. Eimer, J. R. Williamson, S. G. Boxer, R. Pecora, *Biochemistry* **29**, 799 (1990).
20. T. Tao, *Biopolymers* **8**, 609 (1969).
21. P. J. Hagerman, *Biopolymers* **20**, 1503 (1981).
22. S. Diekmann, W. Hillen, B. Morgeneyer, R. D. Wells, D. Porschke, *Biophys. Chem.* **15**, 263 (1982).
23. We are grateful to M. Goulian for a careful reading of this manuscript. This work is supported by the MRSEC grant DMR-0520020 and NSF grant DMR-0505048.

α-Hydroxy and α-Amino Acids Under Possible Hadean, Volcanic Origin-of-Life Conditions

Claudia Huber[1] and Günter Wächtershäuser[2]*†

To test the theory of a chemoautotrophic origin of life in a volcanic, hydrothermal setting, we explored mechanisms for the buildup of bio-organic compounds by carbon fixation on catalytic transition metal precipitates. We report the carbon monoxide–dependent formation of carbon-fixation products, including an ordered series of α-hydroxy and α-amino acids of the general formula R-CHA-COOH (where R is H, CH_3, C_2H_5, or $HOCH_2$ and A is OH or NH_2) by carbon fixation at 80° to 120°C, catalyzed by nickel or nickel,iron precipitates with carbonyl, cyano, and methylthio ligands as carbon sources, with or without sulfido ligands. Calcium or magnesium hydroxide was added as a pH buffer. The results narrow the gap between biochemistry and volcanic geochemistry and open a new gateway for the exploration of a volcanic, hydrothermal origin of life.

The theory of a volcanic, hydrothermal, chemoautotrophic origin of life postulates a locally and temporally coherent, evolvable system of autocatalytic, synthetic carbon-fixation pathways, catalyzed by inorganic transition metal precipitates (1–4) and generating low molecular weight organic compounds from highly oxidized precursors. Here, this system of pathways is termed "pioneer metabolism." In accordance with the principle of metabolic continuity, the theory assumes a step-by-step evolutionary changeover by evolution of ligand feedback from racemic ligands of the inorganic transition metal precipitates to homochiral metal-loenzymes of extant organisms (3, 4). In a continuing effort to establish an experimental grounding for this hypothesis, we experimentally explored the viability of volcanic, hydrothermal carbon-fixation pathways using CO and CN⁻ as carbon sources.

We chose Ni or Ni,Fe precipitates as catalytic transition metals because of the catalytic roles of these biometals (as sulfide or hydroxide complexes) in our previous experiments (5, 6); (Ca, Mg)(OH)₂ as source for hydroxy ligands and for buffering against acidification; Na₂S or CH₃-SNa as sources for sulfido or methylthio ligands; and CO and KCN as sources for carbonyl and cyano ligands in accordance with extant [Fe,Ni]- and [Fe,Fe]-hydrogenases (7).

The reaction conditions are listed in Table 1. Unless stated otherwise, the experiments were carried out in a slurry with 10 ml of H₂O and ¹³C-labeled KCN (8). The alkaline pH range is in agreement with the pH requirement of peptide synthesis (6). The range of reaction temperatures was chosen in agreement with previous experiments (5, 6) and within the range of growth temperatures of hyperthermophiles. The CO gas pressure of 1 bar was chosen as in previous experiments (5, 6) and combined with a reaction time of 10 days (run 1). In other runs, the reaction time was shortened (and product yields increased) by an increase of CO gas pressure. The pH was measured at the end of the reaction. Products in the supernatant were analyzed after freeze-drying by gas chromatography–mass spectroscopy (GC-MS).

α-Hydroxy and α-amino acids as main products (Table 1) constitute ordered series defined by the general formula R-CHA-COOH, where R is H, CH₃, CH₃-CH₂, or HO-CH₂ and A is OH or NH₂. Temperature increase correlates positively with product yield and with the ratio of amino acids to hydroxy acids. The replacement of H₂O by D₂O leads to deuterated products. With ¹³C-labeled KCN, we discriminated cyano ligands from CO (and, optionally, methylthio) ligands as the carbon source. The resulting isotopomers revealed a rich and complex system of pathways involving all-cyano, all-noncyano, and combined cyano/noncyano ligands, as exemplified by ratios of ¹²C₃:¹³C₃ isotopomers for lactate and alanine. The contribution by noncyano pathways correlates positively with a decrease in CO gas pressure and an increase in temperature. This multiplicity of pathways may facilitate metabolic evolution and a stepwise changeover from a Ni-dependent use of CO and/or cyano ligands without energy coupling to a sole use of CO₂ with energy coupling. We also detected α-hydroxy-*n*-valeric acid (run 4, 0.005 μmol), α-hydroxy-*i*-valeric acid (runs 4 and 5, trace amounts), and α-amino-*n*-valeric acid (run 4, trace amount). The progressive chain elongation suggests long-chain α-hydroxy or α-amino acids as primordial lipids.

Added ¹⁵N-NH₃ enters the amino acids, which suggests the participation of a pool of ammonia. The replacement of KCN in run 3 by glycine and alanine generated α-hydroxy acids at very low rates. This means that α-amino and α-hydroxy acids are mainly competitive products and, to a minor extent, consecutive products. The detection of glycine amide by high-performance liquid chromatography (HPLC)–MS (8) suggests carboxamides as intermediates between CN and COOH groups. The detection of pyruvate (runs 3, 4, 5, and 10) having a similar isotopomer ratio as lactate and alanine suggests α-keto and α-imino groups as intermediates.

Acetate, propionate, and butyrate (in varying isotopomer ratios) have been detected with yields decreasing in that order. The detected ethylene

[1]Department of Organic Chemistry and Biochemistry, Technische Universität München, Lichtenbergstraße 4, D-85747 Garching, Germany. [2]Weinstraße 8, D-80333 München, Germany.

*Present address: 209 Mill Race Drive, Chapel Hill, NC 27514, USA.

†To whom correspondence should be addressed. E-mail: gwmunich@yahoo.com